CHEMISTRY
A EUROPEAN JOURNAL

DOI: 10.1002/chem.200700658

The Valence Problem of $Pd_4Br_4Te_3$

Manuel Janetzky,[a] Eva Rödel,[b] Clemens Pietzonka,[a] Ulrich Müller,[a] Thorsten Ressler,[c] and Bernd Harbrecht*[a]

Dedicated to Professor Dieter Fenske on the occasion of his 65th birthday

Abstract: $Pd_4Br_4Te_3$ was prepared from Pd, Te, and $PdBr_2$ at 700 K. Its structure was determined by single-crystal X-ray diffraction to be triclinic, $P\bar{1}$, Pearson symbol $aP22$; $a=842.5(2)$, $b=845.0(3)$, $c=864.8(3)$ pm; $\alpha=82.55(3)$, $\beta=73.36(2)$, $\gamma=88.80(2)°$; $Z=2$. The Br and Te atoms are arranged according to the motif of cubic closest-packed spheres in which every 15th position is vacant; the Pd atoms occupy 8/15 of the octahedral voids. The symmetry relations with the packing of spheres are derived. Prominent structural units are hollow cuboctahedral $[(PdBrTe)_6]$ units, the Pd atoms are positioned near the centers of the square faces of the Br_6Te_6 cuboctahedra; the cuboctahedra and double-octahedral $Pd_2Br_4Te_6$ units are connected to strands by sharing triangular Te_3 faces. The strands are condensed by common Br atoms into layered assemblies. Conspicuously close Te–Te contacts in the Te_3 triangles indicate attractive Te–Te interactions. The valence puzzle is resolved by the formula $Pd(+II)_4Br(-I)_4Te(-4/3)_3$. Positive Te–Te Mulliken orbital populations and the Pd–K, Br–K, and Te–L_{III} XANES spectra of $Pd_4Br_4Te_3$ referenced to the spectra of $PdBr_2$, K_2PdBr_6, PdTe, and $PdTe_2$ are in accord with attractive Te–Te interactions. The measured semiconducting and diamagnetic properties are compatible with the derived picture of chemical bonding in $Pd_4Br_4Te_3$.

Keywords: electronic structure · palladium chalcogenide halides · solid-state structures · tellurium · X-ray absorption spectroscopy

Introduction

Low-temperature solvothermal synthesis has proven to be a fruitful preparative method for gaining access to ternary chalcogen halogen compounds of the platinum group metals with unforeseen structural features and intricate bonding interactions and physical properties.[1–10] Halogen-rich compounds, as for instance $[PdBr_2(TeBr_2)_2]$[1] or $[PtCl_4(SeCl_4)_2]$,[2] exhibit neutral chalcogen di- or tetrahalide species coordinating to the metal atoms, whereas phases that contain less halogen, for example, $[Pd_8Cl_8(S_2)_4]$,[3] $[Pd_6Cl_6(S_2)_3]$[4] or $[Pd_4I_6Se_2]$[5] usually contain dichalcogenide dumbbells. If the phases are rich in chalcogen, like $[PdCl_2Se_6]$,[6] $[PdBr_2Se_6]$,[6,7] or $[PdCl_2Se_8]$,[8] neutral chalcogen moieties are coordinating to the metal atoms. "Ordinary" chalcogenide halides like PdITe[5,9] have been found to be electronic conductors. In spite of its diamagnetic properties, PdITe reputedly contains Pd in oxidation state (+III), which is unknown for the binary platinum group metal chalcogenides or halides: PtX_3 (X = Cl, Br, I) are mixed-valent (+II/+IV) halides.[11–15] Some related noble metal chalcogenide halides exhibit mixed electron- and ion-conducting properties.[16] Most of the phases identified so far were prepared by solvothermal routes using halogen,[10] chalcogen halide[3] or a concentrated aqueous hydrohalic acid[9] as liquid phase.

We became aware of noble metal chalcogenide halides in the course of our search for a suitable transport agent to promote the growth of Pd-rich telluride crystals by a chemical vapor transport reaction. $PdBr_2$[17–19] and $PdCl_2$[17,20] proved to be suitable agents to enable controlled access to crystals of the various phases accommodated in the Pd-rich region of the Pd–Te system.[21–26] In spite of a critical comment concerning unsuccessful attempts to synthesize plati-

[a] M. Janetzky, C. Pietzonka, Prof. U. Müller, Prof. B. Harbrecht
Fachbereich Chemie und Wissenschaftliches Zentrum
für Materialwissenschaften
Philipps-Universität, 35032 Marburg (Germany)
Fax: (+49) 6421-28-28917
E-mail: harbrecht@chemie.uni-marburg.de

[b] Dr. E. Rödel
Fritz-Haber-Institut der Max-Planck-Gesellschaft
14195, Berlin (Germany)

[c] Prof. T. Ressler
Institut für Chemie, Technische Universität Berlin
10623, Berlin (Germany)

num group metal chalcogenide halides from elements or binaries,[6] we investigated the Pd/Te/$PdBr_2$ system at enhanced $PdBr_2$ amounts and reduced temperatures compared with the vapor-transport conditions for the crystal growth of Pd-rich tellurides. We report now, the structural and physical properties of $Pd_4Br_4Te_3$. To our knowledge, $Pd_4Br_4Te_3$ is the first example of a palladium chalcogenide halide produced by conventional solid-state synthesis. Furthermore, we provide experimental evidence that the valence puzzle inherent to the composition of $Pd_4Br_4Te_3$ originates from weak homonuclear Te–Te interactions associated with partly unoccupied Te p states.[27]

Synthesis, phase analysis, and chemical properties of $Pd_4Br_4Te_3$: $Pd_4Br_4Te_3$ forms readily from mixtures of appropriate amounts of Pd, Te, and $PdBr_2$ in previously outgassed, sealed quartz glass ampoules at 700 K within three days in the form of black polyhedral crystals that exhibit a silvery luster, see Figure 1. Up to 2 mm^3 sized crystals could be grown that way. A temperature gradient of 30 K along the reaction tube in the 600–700 K range was found to be ineffective with regard to increased size or improved quality of the crystals. $Pd_4Br_4Te_3$ is also accessible at otherwise similar conditions from a mixture of PdTe, $PdTe_2$, and $PdBr_2$ blended in the amount-of-substance ratio 1:1:2. Deviations from this ratio yield phase mixtures. The same heat treatment of 1:1:1 and 1:1:4 mixtures also yields $Pd_4Br_4Te_3$, however, with admixtures of tellurides and $PdBr_2$, respectively. Excess $PdBr_2$ can be removed with an aqueous solution of KBr; $Pd_4Br_4Te_3$ is not attacked. A series of analyses by energy dispersive X-ray spectroscopy (EDXS) resulted in relative amounts of substance of 36(2)% Pd, 35(3)% Br, and 28(2)% Te. The values are in fair agreement with $Pd_4Br_4Te_3$ corresponding to 36.36% Pd, 36.36% Br, and 27.27% Te. Within the limits of the accuracy of the method no other elements with atomic numbers $Z \geq Z(\mathrm{Na})$ were detected in the sample. Small deviations from the element 4:4:3 ratio during synthesis lead to the formation of by-products. Thus, we conclude that the phase does not tolerate substantial deviations from the composition $Pd_4Br_4Te_3$ (see Table 3 in the Experimental Section). Upon heating above 800 K, $Pd_4Br_4Te_3$ decomposes into a reddish brown amorphous solid which can be quenched to ambient temperature. Analysis by using EDXS shows that the transformation occurs without perceptible change of composition. All prepared samples were investigated by X-ray powder diffractometry. A pseudo-Voigt profile fit to a diffraction pattern of single phase $Pd_4Br_4Te_3$ is shown in Figure 2.

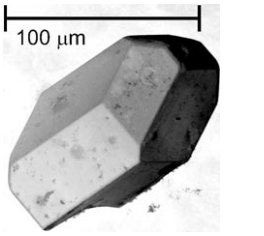

Figure 1. Scanning electron microscope image of a crystal of $Pd_4Br_4Te_3$.

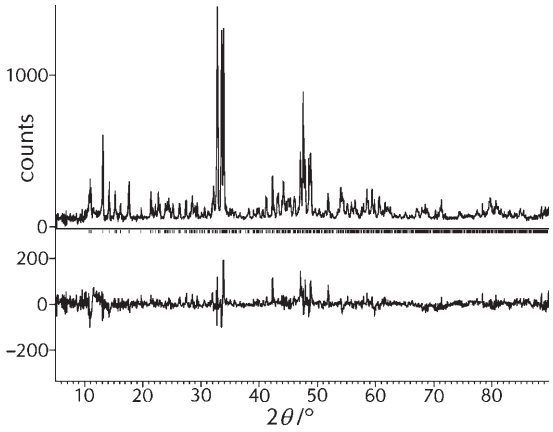

Figure 2. Rietveld fit to an X-ray powder diffraction pattern ($Cu_{K\alpha}$) of $Pd_4Br_4Te_3$.

Physical properties: According to four-point d.c. measurements $Pd_4Br_4Te_3$ is a semiconductor. As seen from Figure 3, the resistivity of a compressed powdered sample was found to vary between 30 and 40 Ωm in the temperature range 300–50 K. The small change and non-exponential decay of the resistivity with increasing temperature indicates that the electron transport in the mentioned temperature range is not controlled by the thermally activated processes that usually apply to semiconductors.

Magnetization measurements in the temperature range 2–300 K and a magnetic field of 3 T (Figure 4) reveal that the core diamagnetism of the constituents of $Pd_4Br_4Te_3$ ($-4.4 \times 10^{-9}\ m^3 mol^{-1}$)[28] dominates the magnetic properties in the measured temperature range 2–300 K. Accordingly, Pd has

Abstract in German: *$Pd_4Br_4Te_3$ wurde aus Pd, Te und $PdBr_2$ bei 700 K hergestellt. Nach der Strukturanalyse mittels Einkristall-Röntgenbeugung kristallisiert es triklin, P$\bar{1}$, Pearson-Symbol* aP22*;* a = *842,5(2),* b = *845,0(3),* c = *864,8(3) pm;* α = *82,55(3),* β = *73,36(2),* γ = *88,80(2)°;* Z = *2. Die Br- und Te-Atome sind nach dem Muster einer kubisch-dichtesten Kugelpackung angeordnet, in der jede 15-te Position unbesetzt ist; die Pd-Atome besetzen 8/15 der Oktaderlücken. Die Symmetriebeziehungen zur Kugelpackung werden hergeleitet. Im Zentrum unbesetzte, kuboktaedrische $[(PdBrTe)_6]$-Baugruppen sind mit $Pd_2Br_4Te_6$-Doppeloktaedern über gemeinsame dreieckige Te_3-Flächen zu Strängen verknüpft, die ihrerseits über gemeinsame Br-Atome zu Schichten angeordnet sind. Auffällig kurze Te–Te-Kontakte in den Te_3-Dreiecken deuten auf attraktive Te–Te-Wechselwirkungen hin. Die zunächst rätselhafte Valenzsituation wird durch die Formulierung $Pd_4^{(+II)}Br_4^{(-I)}Te^{(-4/3)}_3$ gedeutet. Positive Te–Te-Mulliken-Orbital-Populationen und die Pd–K-, Br–K- und Te–L_{III}-XANES-Spektren von $Pd_4Br_4Te_3$ im Vergleich zu den Spektren von $PdBr_2$, K_2PdBr_6, PdTe und $PdTe_2$ bestätigen die attraktiven Te–Te-Wechselwirkungen. Die gemessenen halbleitenden und diamagnetischen Eigenschaften von $Pd_4Br_4Te_3$ passen zu dem abgeleiteten Bindungsmodell.*

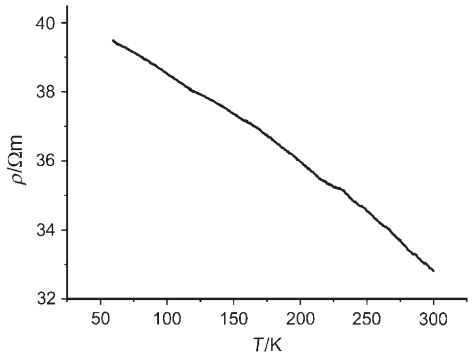

Figure 3. Resistivity as a function of temperature for $Pd_4Br_4Te_3$.

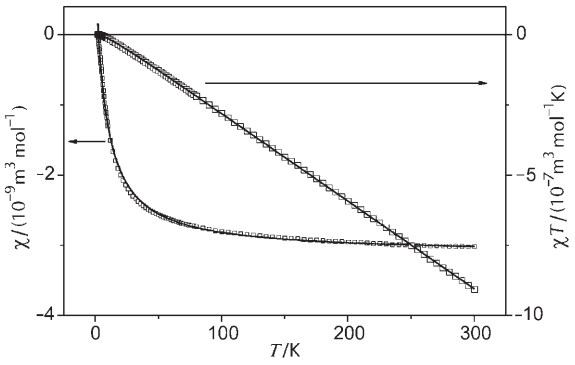

Figure 4. Magnetic susceptibility χ (left scale) and χT (right scale) as a function of temperature for $Pd_4Br_4Te_3$.

an even number of d electrons in a low spin configuration, excluding the presence of trivalent palladium. At low temperatures a moderate hyperbolic increase of the susceptibility with decreasing temperatures indicates a small temperature dependent paramagnetic contribution. Figure 4 shows numerical fits of χ versus T and $T\chi$ versus T including a temperature independent diamagnetic and a temperature dependent Curie–Weiss term. According to the latter fit, the diamagnetic contribution amounts to $-3.128(3)\times 10^{-9}\,m^3\,mol^{-1}$. From the Curie constant of the fit χ vs. T we obtain an effective moment of 0.145(1) μ_B per formula unit and −8.1(2) K for the Weiss constant.

Crystal structure: $Pd_4Br_4Te_3$ crystallizes in the triclinic space group $P\bar{1}$ with 11 crystallographic distinct atoms and 22 atoms per unit cell. As shown in the left part of Figure 5, every one of the atoms Pd1, Pd2, and Pd3 is coordinated by two Br and two Te atoms in a slightly distorted *cis*-square-planar configuration. Pseudo-square-planar $PdBr_2Te_2$ units are condensed to $[(PdBr_{2/2}Te_{2/2})_6]$ units. In these units, the Br and Te atoms occupy the vertices of a pseudo-cuboctahedron and the Pd atoms are located close to the centers of its square faces. Similar pseudo-cuboctahedral units have been found in other cluster compounds like $[(PtCl_2)_6]$ in β-$PtCl_2$,[29] the 12 e cluster compound of the high temperature polymorph γ-ZrI_2,[30] and in ternary reduced niobium and tantalum oxides like $K_2Ta_{15}O_{32}$.[31] $Pd_4Br_4Te_3$ differs from the mentioned halides in that the pseudo-cuboctahedral unit

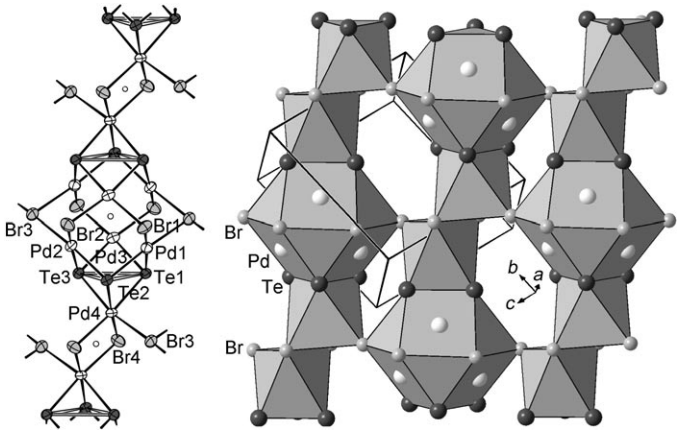

Figure 5. Structural characteristics of $Pd_4Br_4Te_3$. Left: Section of a strand of face-sharing pseudo-cuboctahedral and double-octahedral units depicting covalent bonds and ellipsoids of thermal motion (67% probability at 20°C); small circles mark inversion centers. Right: Three linked strands forming a layer parallel to (101) shown from the same direction of view.

shares its two opposite Te_3 faces with distorted octahedral $PdBr_3Te_3$ units around Pd4. The resulting larger units are condensed into strands by common octahedron edges made up from the Br4 atoms. In the strand, pseudo-cuboctahedral and double-octahedral units alternate. The strands are condensed into layers by common Br3 atoms coordinating Pd atoms of both, the cuboctahedral (255.8 and 257.5 pm) and the double-octahedral units (280.6 pm) (cf. Figure 5 right). Between the layers, which are oriented parallel to (101), the cohesion appears to be weak: no interatomic distance between layers is shorter than $d(Pd2{-}Br2) = 329.1$ pm.

The arrangement of the Br and Te atoms corresponds to the motif of a cubic closest-packing of spheres, albeit with every 15th sphere site vacant. The vacancies are located at the inversion centers at 1/2,1/2,0 in the centers of the pseudo-cuboctahedral $[(PdBr_{2/2}Te_{2/2})_6]$ units. Each unoccupied site is encapsulated by a hexagon of six bromine atoms and two adjacent Te_3 triangles. The Pd atoms occupy 8 out of 15 octahedral voids of the packing of spheres. The formula of the compound can thus be stated as $Pd_8\square_7Br_8Te_6\boxtimes$, □ referring to the octahedral voids and ⊠ to the vacant sphere positions. The vacant sphere position is one of the "vertices" of the coordination "octahedra" around Pd1, Pd2, and Pd3; these Pd atoms attain a 4+1 coordination (2 Te ligands at 253 pm, 2 Br at 250–257 pm, 1 Br or Te at 329–333 pm). The Pd4 atoms have a 5+1 coordination (Table 1).

The "hexagonal" sheets of spheres that are parallel to $(11\bar{1})_c$ of the face-centered cubic cell correspond to sheets parallel to $(12\bar{1})_t$ of the triclinic cell. Within these sheets the Br and Te atoms are segregated in ribbons that run in the direction $[\bar{1}11]_t$, that is, from right to left in Figure 6. This enables specific distortions of the structure. We shall have a closer look at this feature and the coordination of the various Pd atoms when we analyze the valence problem inherent to the composition $Pd_4Br_4Te_3$.

The translational symmetry of the compound is defined by the distribution of the defects. In the chosen setting they

Table 1. Interatomic distances in pm and integrated Mulliken overlap populations for $Pd_4Br_4Te_3$.

Atom1	Atom2	distance	COOP
Pd1	Br1	250.4(1)	0.32732
	Te2	253.1(1)	0.40708
	Te1	253.3(1)	0.40440
	Br3	255.8(1)	0.30287
	Te1	333.8(1)	0.02783
Pd2	Te2	252.0(1)	0.39471
	Br2	252.7(1)	0.31888
	Te3	253.1(1)	0.39629
	Br3	257.5(1)	0.27627
	Br2	329.1(2)	0.01679
Pd3	Br1	251.2(1)	0.32890
	Te3	251.9(1)	0.40979
	Br2	252.3(1)	0.31875
	Te1	252.7(1)	0.38570
	Br1	331.6(1)	0.00562
Pd4	Br4	257.0(1)	0.30127
	Te1	259.5(1)	0.33585
	Te2	260.0(1)	0.32060
	Br4	260.2(1)	0.28796
	Te3	261.7(1)	0.30166
	Br3	280.7(1)	0.15715
Te1	Te3	325.9(1)	0.03582
	Te2	331.7(1)	0.00919
Te2	Te3	321.9(1)	0.05846

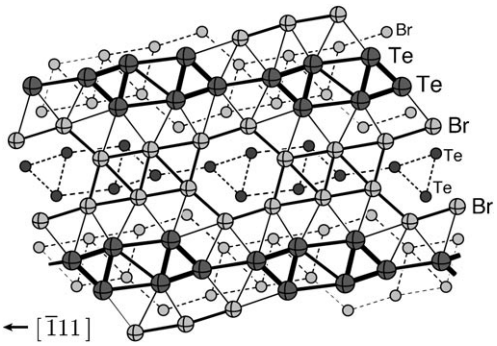

Figure 6. Ordering of the Te and Br atoms and vacancies in ribbons within a "hexagonal" sheet parallel to $(11\bar{1})_c$ of a face-centered cubic packing of spheres. Plan view of a sheet parallel to $(12\bar{1})_t$ of the triclinic cell of $Pd_4Br_4Te_3$. Small circles mark atomic positions of the next sheet.

are located on the inversion centers at 1/2,1/2,0. Figure 7 highlights the orientation relation between the triclinic cell and the associated hypothetic cubic lattice. The basis vectors of the triclinic cell result from those of the face-centered cubic cell by the following transformation matrix P in Equation (1):

$$(a_t, b_t, c_t) = (a_c, b_c, c_c)\mathrm{P};\ \mathrm{P} = \begin{pmatrix} 3/2 & 1/2 & 1/2 \\ -1/2 & 3/2 & 0 \\ 0 & 0 & 3/2 \end{pmatrix} \quad (1)$$

The space group of $Pd_4Br_4Te_3$ must be a subgroup of $Fm\bar{3}m$, the space group of the packing of spheres, which we

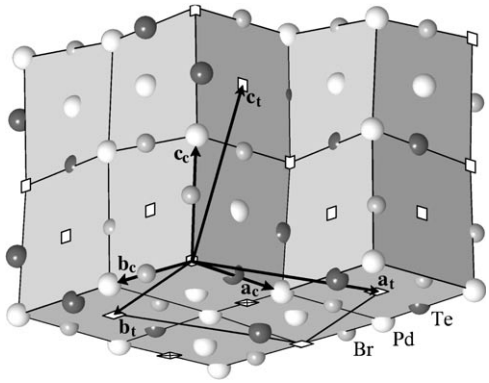

Figure 7. Relation between the orientations of a devised cubic and the real triclinic unit cell. The Schottky symbol □ represents an unoccupied octahedral site, ⊠ a vacancy in the packing of spheres.

take to be the aristotype. The translational part of the group-subgroup index corresponds to the determinant $|\mathrm{P}| = 3.75$ of the matrix P. The transformation includes a change from a face-centered to a primitive lattice, therefore, the value of $|\mathrm{P}|$ has to be quadrupled to $4\times|\mathrm{P}| = 15$. Furthermore, the transformation is associated with a complete loss of non-trivial rotational symmetry totaling a gain of 24 additional degrees of freedom. Thus, the index of the symmetry reduction from the cubic closest-packing of spheres amounts to $15\times24 = 360$. The symmetry relations from $Fm3m$ to the space group $P\bar{1}$ of $Pd_4Br_4Te_3$ are depicted as a Bärnighausen tree[32,33] in Figure 8. The Figure also shows how the Wyckoff positions of $Pd_4Br_4Te_3$ result from those of the cubic closest-packing of spheres.[34] Comparison with the parameters listed in Table 5 in the Experimental Section, affords an estimate of the degree of distortion of the real structure. In addition, there are metrical distortions of the crystal lattice. Assuming $a_c = 538.1$ pm for the lattice parameter of the cubic aristotype, one calculates $a_t = b_t = c_t = 850.8$ pm and $\alpha_t = 84.3$, $\beta_t = 72.5$, and $\gamma_t = 90°$ for the undistorted triclinic structure, as compared to the actual values of $a = 842.0$, $b = 845.7$, and $c = 865.5$ pm, and $\alpha = 82.52$, $\beta = 73.38$, and $\gamma = 88.80°$. The derived symmetry relations refer to a structure-type correlation and, of course, do not have any further physical significance.

The valence problem of $Pd_4Br_4Te_3$ and its solution: The composition of the title compound is incompatible with common oxidation states for all constituents, i.e., Pd(+II), Br(−I), Te(−II). If we assume that the most electronegative component Br holds oxidation state (−I), three solutions are possible: either some Pd atoms adopt oxidation state (+IV), and/or Te is not completely reduced. Incomplete reduction without formation of Te(−II) dumbbells is found for several transition metal ditellurides MTe_2 (M = Ni, Rh, Ir, Pd, Pt).[35] In the following, we analyze the valence problem in three respects: Firstly, we compare relevant interatomic distances with those in selected Pd compounds with well defined valence states. Secondly, we perform extended Hückel

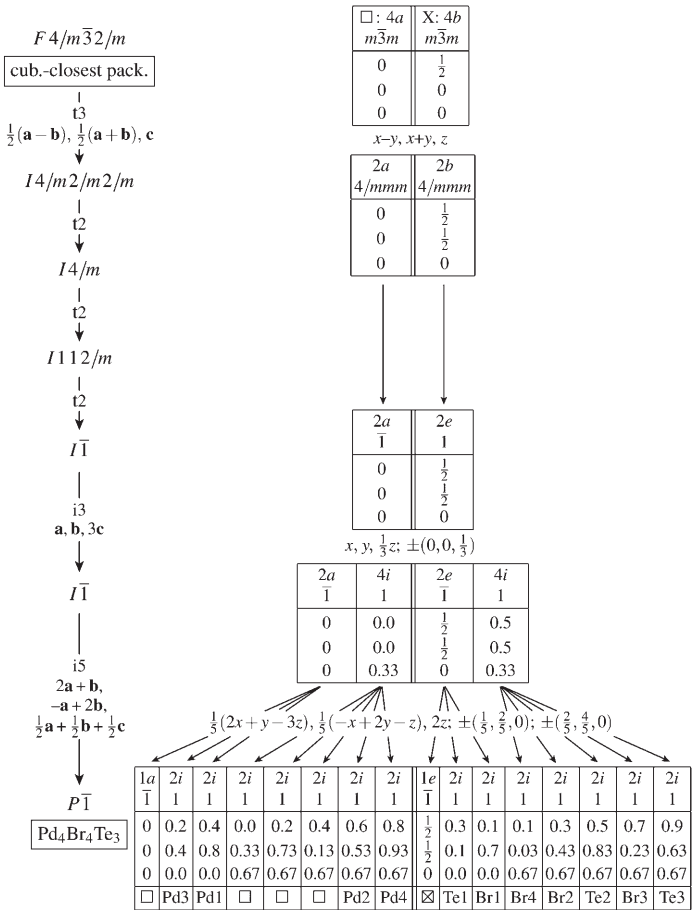

Figure 8. Group-subgroup relations between the space groups of a cubic closest-packing of spheres and $Pd_4Br_4Te_3$. t3 = *translationengleiche* subgroup of index 3, i5 = isomorphic subgroup of index 5. Boxes contain: Wyckoff position, site symmetry and the ideal atomic coordinates for an undistorted packing of spheres. The Schottky symbol □ represents an unoccupied octahedral site, ⊠ a vacancy in the packing of spheres.

calculations and analyze the results with respect to specific Te–Te interactions and thirdly, we provide evidence for the localization of unusual valence states in the Te substructure as a result of a comparative XANES study.

Comparative analysis of interatomic distances: The distorted square planar coordination of Pd1, Pd2, and Pd3 with a fifth neighbor at remote ≈330 pm is consistent with the valence state (+II) for these Pd atoms. These Pd–Br distances of $Pd_4Br_4Te_3$ (250.4 to 257.5 pm) are even somewhat longer than in $PdBr_2$ (2×242.2 and 2×242.8 pm)[19] or the corresponding distances in mixed-valent $PtBr_3$ (4×≈244, 1×290 pm).[15] The Pd–Te distances (251.9 to 253.3 pm) are about the same as in $PdBr_2(TeBr_2)_2$ (2×≈252 pm).[1] Pd4 with its 5+1 coordination could be a candidate for Pd(+IV). The distances (3×Br: 257.0, 260.0, 280.7 pm, 3×Te: 259.5, 260.2, 261.7 pm), however, are considerably longer than those of Pt(+IV)–Br in $PtBr_3$ (6×253.7 to 256.3 pm) or in K_2PdBr_6 (6×245.9 pm).[36] Therefore, the oxidation state (+IV) is unlikely for Pd4. The diamagnetic properties of $Pd_4Br_4Te_3$ rule out d^7 configurated Pd(+III).

The Te and Br atoms are not equally dispersed but segregated in ribbons of defective close-packed atomic layers (Figure 6). Nevertheless, the size of the van der Waals radii of Br and Te (185 and 206 pm)[37] match fairly well with the mean distance of the atoms in the defective close packing (380.4 pm). The shortest homoatomic separations, however, differ drastically: d(Te2–Te3) = 321.9 pm compared to d(Br1–Br3) = 366.1 pm. The short Te–Te contacts occur in Te_3 triangles. All three distances, 321.9, 325.9, and 331.7 pm, are significantly closer to twice the covalent radius (274 pm)[38] than twice the van der Waals radius (412 pm). Moreover, the Te–Pd–Te angles are reduced from ideal 90° to about 80°. Based on the ratio of the sizes of the covalent atomic radii (r(Te) = 137 pm, r(Br) = 114 pm)[38] and the van der Waals radii we would expect a shrinkage of the Br–Pd–Br instead of the Te–Pd–Te angles. Thus, we conclude the presence of attractive Te–Te interactions associated with incomplete reduction of Te. Similar Te–Te interactions are also indicated for paramagnetic $IrTe_2$ with d^5 configurated Ir(+III) and Te(−3/2), Te–Te (349.7 and 355.8 pm).[35] An oxidation state of −4/3 instead of (−II) for Te in $Pd_4Br_4Te_3$ would be compatible with the short Te–Te distances and resolve the puzzle of the valences.

Extended Hückel calculations: In order to critically check the hypothesis of attractive Te–Te interactions we performed extended Hückel calculations. The lower part of Figure 9 shows the total density of states (DOS) and its dis-

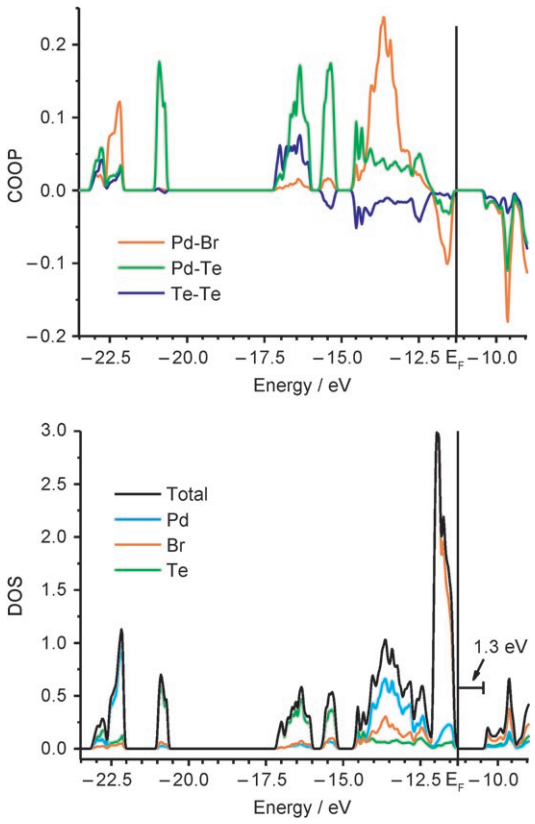

Figure 9. Crystal orbital overlap populations COOP (top), density of states DOS and partial densities of states of $Pd_4Br_4Te_3$.

section into the partial densities (pDOS) of the three contributors. The crystal orbital overlap populations (COOP) Pd–Br, Pd–Te, and Te–Te ($d \leq 400$ pm) are depicted in the upper part of Figure 9. Mulliken overlap population values calculated for $d \leq 340$ pm are listed in Table 1. The DOS diagram displays essentially four features in the energy range −17.5 eV up to the Fermi energy E_F at −11.3 eV. According to the COOP, the DOS in this region reflects predominantly constructive Pd–Te and Pd–Br interactions, the former energetically more dispersed and located at lower energy than the latter. Consequently, and as indicated by the Mulliken overlap population values (Table 1), the Pd–Te interactions are stronger than the Pd–Br interactions. Only small portions of these COOPs close to E_F are negative. Moreover, part of the Te p states are used for homonuclear Te–Te interactions, attractive in the range between −17 to −15.5 eV, repulsive and more strongly dispersed at higher energies. More important, not all anti-bonding Te–Te states are occupied: a small portion is located above the Fermi level. This evidences incomplete reduction of Te in $Pd_4Br_4Te_3$, a prerequisite for overall attractive Te–Te interactions. They are numerically reflected in small, but positive Mulliken overlap population values varying between 0.009 and 0.058 (Table 1).

XANES spectroscopy: In order to gain further insight in the electronic structure of $Pd_4Br_4Te_3$, X-ray absorption near edge structure (XANES) spectra at the Pd–*K*, Br–*K*, and Te–L_{III} edges were recorded for $Pd_4Br_4Te_3$, PdTe,[39] $PdTe_2$,[40] $PdBr_2$,[17–19] and K_2PdBr_6.[36] The spectra of the last four compounds were used as standards for Te(−II), Te(−I), Pd(+II), and Pd(+IV). The energy of a specific X-ray absorption edge for a given atom generally depends on the electronic state, i.e., the specific chemical surrounding of the respective atom. The energy of a given absorption edge of an atom scales with its charge. In favorable cases the edge energy correlates with the oxidation state of the studied species. Usually, valence states are not determined on an absolute but on a relative scale by comparing the XANES spectra of a given absorption edge and atom in chemically varying environments. No detailed EXAFS analysis of the local structures around the various metal atoms was attempted, owing to the high number of distinct crystallographic sites of the crystal structure of $Pd_4Br_4Te_3$.

The XANES spectra at the Pd–*K* edge for the title compound and four reference substances are shown in the upper right part of Figure 10. The vertical lines cut the curves at the inflection points determined as the root of the second derivatives. The energy at the inflection point is chosen as reference. As expected for Pd(+IV) the Pd–*K* edge of K_2PdBr_6 is shifted by 2.5–4.1 eV to higher energy relative to the Pd–*K* edges of the other phases. For exact values we refer to Table 2. The inflection point of the Pd–*K* edge of $Pd_4Br_4Te_3$ is positioned at the low energy side right next to that of PdTe. Thus, a Pd oxidation state of $>(+II)$ can be ruled out. Moreover, we note that the energies of the Pd *K* edges of the various compounds with Pd(+II) vary over a range of 1.5 eV. This energy difference is significantly larger than the impreciseness of the measured photon energies, which is estimated to amount to less than 0.2 eV. Thus, the edge energies also reflect pieces of information concerning distinctions in the polarity of a chemical bond between two given constituents of the various Pd compounds on a relative scale.

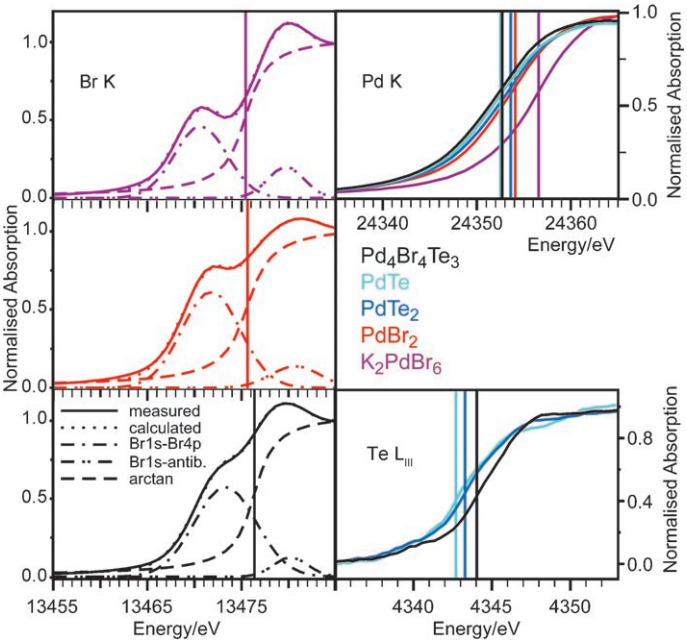

Figure 10. XANES spectra of $Pd_4Br_4Te_3$, PdTe, $PdTe_2$, $PdBr_2$, and K_2PdBr_6 at the Pd–*K*, Te–L_{III}, and Br–*K* edges.

Table 2. Energies in eV of the inflection points of the Pd–*K*, Br–*K*, and Te–L_{III} X-ray absorption edges.

	Pd–*K*	Br–*K*	Te–L_{III}
PdTe	24352.5	–	4342.7
$PdTe_2$	24353.6	–	4343.3
$PdBr_2$	24354.1	13475.6	–
K_2PdBr_6	24356.6	13475.4	–
$Pd_4Br_4Te_3$	24352.7	13476.4	4344.0

The left part of Figure 10 shows the XANES spectra of $Pd_4Br_4Te_3$, K_2PdBr_6, and $PdBr_2$ at the Br–*K* edge. The pre-edge peaks are attributed to a Br 1s to Br 4p transition. This transition is presumably caused by the strong overlap of Br 4p and Pd 4d orbitals enabling ligand to metal charge transfer stimulated by the excitation of the Br 1s electrons.[41] Similar pre-edge features were found in, for example, Ni and Cu oxides (O 2p to metal 3d charge transfer)[42] and rare earth (RE) fluorides (F 2p to RE 4f charge transfer).[43] The post-edge peak can be assigned to electron transfer into antibonding states. The root of the second derivative of the Br–*K* spectra was determined by deconvoluting the spectra with two Gaussians for the pre- and post-edge peaks and an arc tangent function for the shape of the edge. The inflection points of the Br–*K* edges of the two bromides are nearly at the same position whereas the corresponding edge

of $Pd_4Br_4Te_3$ is about 1 eV shifted towards higher energy. Apparently, the electron density at the Br atoms is reduced and thus, the bonding in the bromide telluride is less heteropolar. The latter conclusion is corroborated by small but consistent shifts of the inflection points of the Pd–*K* and Br–*K* edges of $Pd_4Br_4Te_3$ relative to the edge positions of the reference compounds. In turn, the congruence of these subtle features corroborates the consistency and reliability of the data evaluation.

The XANES spectra of PdTe, $PdTe_2$, and $Pd_4Br_4Te_3$ monitored at the L_{III} edge are shown in the lower right part of Figure 10. As expected, the Te-L_{III} edge of PdTe is found at the lowest energy. The edge of $PdTe_2$ containing Te in a less reduced state Te(−I) is shifted by 0.6 eV towards higher energy. The Te-L_{III} edge energy is highest for $Pd_4Br_4Te_3$ and relatively shifted to that in PdTe by 1.3 eV. Thus, the Te atoms in the bromide telluride seem to carry the least negative charge. This shift corroborates the postulated attractive Te–Te interactions indicated by the relatively short Te–Te distances and the positive Mulliken overlap populations. At first view, the pronounced shift even suggests an oxidation state seemingly less negative than that of Te(−I) in $PdTe_2$. The pretended contradiction, however, can be resolved by realizing that both the oxidation state and the degree of heteropolar bonding control the position of the edge energies. Similar to the shift of the Te-L_{III} edge, the differences in height of the absorption edge at ≈4348 eV (i.e. the "white line") corroborate the reduced oxidation state of Te in $Pd_4Br_4Te_3$. Since all measured edge energies of $Pd_4Br_4Te_3$ consistently point to particularly low-charged atoms (Table 2), we suggest that the chemical bonds in the bromide telluride are less polar than in $PdBr_2$ and $PdTe_2$.

Conclusions

1) Solid-state synthesis has been proven to be useful for the preparation of new palladium chalcogenide halides. $Pd_4Br_4Te_3$ is, to our knowledge, the first example of a platinum group metal chalcogenide halide prepared in the absence of a solvent.
2) The triclinic structure of $Pd_4Br_4Te_3$ is based on a motif of densely packed Br and Te atoms with one out of 15 positions being unoccupied. The triclinic lattice is defined by the ordered spatial distribution of vacancies in the Br/Te sublattice. The vacancies are located on the centers of the pseudo-cuboctahedral $[(PdBr_{2/2}Te_{2/2})_6]$ units at 1/2, 1/2, 0. The remaining Pd atoms have a distorted octahedral coordination (3×Br, 3×Te). There is a strict group-subgroup relation of index 360 between the space group symmetry of a cubic closest-packing of spheres ($Fm\bar{3}m$) and that of $Pd_4Br_4Te_3$ ($P\bar{1}$).
3) The puzzle with the valences inherent to the composition $Pd_4Br_4Te_3$ could be resolved by means of a comparative analysis of interatomic distances combined with extended Hückel calculations and a comparative XANES study. The shift of the positions of the inflection points of the Pd–*K*, Br–*K*, and Te–L_{III} absorption edges of $Pd_4Br_4Te_3$ relative to the positions of the respective absorptions edges of PdTe, $PdTe_2$, $PdBr_2$, and K_2PdBr_6 used as standards provide clear evidence that the Te atoms are not fully reduced in $Pd_4Br_4Te_3$. Incomplete reduction of the Te atoms enables weak attractive interactions which are mirrored in positive Te–Te Mulliken overlap populations and conspicuously short Te–Te distances (322–331 pm) between 3 Te atoms arranged in a triangle. The assumption of $Te(-4/3)_3$ resolves the puzzle with the valences in $Pd_4Br_4Te_3$. Moreover, the XANES spectra reveal less polar bonding in the ternary bromide telluride than in the binaries $PdTe_2$ and $PdBr_2$.
4) $Pd_4Br_4Te_3$ is a diamagnetic semiconductor. Although we are not able yet to fully rationalize all details of the temperature characteristics of the magnetization and resistivity of the investigated samples, the measured quantities are essentially compatible with the picture of chemical bonding in $Pd_4Br_4Te_3$ derived from structural data, band structure calculation and XANES spectroscopy.

Experimental Section

Synthesis: The title compound $Pd_4Br_4Te_3$ was prepared on a 300–500 mg scale from appropriate amounts of Pd (powder 99.9%, Merck), Te (lump 99.999+%, Fluka) and palladium dibromide (see below). The components were sealed in a previously degassed evacuated silica tube under reduced pressure of Ar (≈5 Pa). The ampoules were heated to 700 K for 4 days in a tube furnace (Carbolite) with a programmable temperature controller. Hereafter, the ampoules were either quenched in cold water or brought to ambient temperature by cooling the furnace at a rate of 40 $K\,h^{-1}$. Both procedures yield silvery lustrous, coarse crystalline $Pd_4Br_4Te_3$. These crystals are stable against ambient conditions, but are slowly attacked by diluted nitric acid. $PdBr_2$[19] was prepared by oxidizing 2 g of Pd powder in a hot aqueous solution of ≈30 mL HBr (Acros Organics 48% in H_2O pure tech.) and ≈4 mL Br_2 (Acros Organics 99+% extra pure) according to the protocol given in reference [18] Subsequently, the liquid was evaporated. The residual dark claret powder was placed in a corundum crucible and heated in air to 620 K. X-ray powder diffraction proved the sample to be single phase (*C*2/*c*; *mC*12; $a=1291.1(8)$, $b=395.6(2)$, $c=658.7(3)$ pm; $\beta=102.49(3)°$). Pristine PdTe[39] (0.5 g; $P6_3/mmc$; *hP*4; $a=414.34(3)$, $c=566.09(5)$ pm) was prepared from equimolar amounts of Pd and Te at 900 K in a degassed, sealed silica ampoule. Subsequently, the product was annealed at 700 K for 6 d. Pristine $PdTe_2$[40] (0.5 g; $P\bar{3}m1$; *hP*3; $a=403.18(3)$, $c=513.70(4)$ pm) was prepared from stoichiometric amounts of the elements according to the protocol given for PdTe. K_2PdBr_6, (300 mg) was prepared by heating 51 mg of Pd powder in ≈15 mL of aqueous HBr containing ≈3 mL of Br_2, until all Pd was dissolved. The solution was allowed to cool for a few minutes and then an aqueous KBr solution containing 57 mg of KBr was added. The precipitate was separated from the solution, washed with water and dried. The X-ray powder diffraction pattern could be refined on the basis of a K_2PtCl_6-type structure:[44] $Fm\bar{3}m$; *cF*36; $a=10.226(2)$ pm.

Scanning electron microscopy (SEM) and energy dispersive analysis of X-rays (EDXS): The morphology of the crystals was examined by employing a scanning electron microscope (CS 4DV, CamScan, 25 kV). EDXS was performed by using a spectrometer (EDXS, Si(Li) detector, Noran Instruments) attached to the microscope. Several samples were analysed by using the Pd–*L*, Te–*L*, and Br–*K* X-ray emission lines for quantification.[45]

Table 3. Technical data of Rietveld refinement of a powder $Pd_4Br_4Te_3$. Pattern see Figure 2.

scan-range 2θ [°]		5–90
time per step/step size [°]		8/0.05
radiation		$Cu_{K\alpha}$
number of variables		18
zero point		0.189(3)
profile fit		pseudo-Voigt
temperature [K]		293(2)
a [pm]		842.0(1)
b [pm]		845.7(1)
c [pm]		865.5(1)
α [°]		82.52(1)
β [°]		73.38(1)
γ [°]		88.80(1)
U		0.17(3)
V		-0.13(2)
W		0.036(3)
asymmetry parameter		1.2(1)
parameter 1		1
parameter 2		−0.018(3)
parameter 3		0.00025(5)
R (expected)		0.09378
R (profile)		0.11461
R (weighted profile)		0.15561
R (Bragg)		0.06826
lattice parameters obtained from other educt mixtures:		
$PdBr_2$/PdTe/$PdTe_2$	2/1/1	4/1/1
a [pm]	842.12(8)	842.3(2)
b [pm]	844.73(9)	844.8(2)
c [pm]	864.99(9)	865.0(3)
α [°]	82.538(7)	82.53(2)
β [°]	73.332(9)	73.32(3)
γ [°]	88.875(6)	88.86(2)

Magnetization and resistivity measurement: Magnetic data were recorded by means of a SQUID magnetometer (MPMS R2, Quantum Design) at temperatures ranging from 2–300 K at an applied magnetic field of 1–3 T. Two differently prepared samples were measured (masses 280.89, 96.07 mg). The diamagnetic contribution of the sample holder made from gelatine was subtracted. The corrected susceptibility data χ versus T and $T\chi$ versus T were fitted by taking into account both a temperature-independent diamagnetic and paramagnetic and a temperature-dependent Curie–Weiss term. The effective moment μ_{eff} (in μ_B) was calculated from the Curie constant. For comparison, the core diamagnetic contributions of the constituents were calculated on the basis of the Pascal constants of Pd(+II), Br(−I), and Te(−II).[28] The data were evaluated for the largest sample (280.89 mg), see Figure 4. The results conform essentially with those obtained for the second sample. The electrical resistance of a compressed rod (2×2×12 mm) was measured in the temperature range 20–320 K by employing a four probe method in the d.c. mode.[46] Four silver wires (diameter: 0.050 mm) were attached to the rod with use of a conductive lacquer coat. The voltage was measured at constant current (100 mA) and temperature (±0.2 K) between the inner two contacts. The temperature was changed stepwise by increments of 1 K. The resistivity ρ was calculated by multiplying the electrical resistance with the ratio of cross sectional area and the distance between the two inner contacts.

X-ray absorption near edge structure (XANES) spectroscopy: The measurements were performed in transmission mode at HASYLAB (Hamburg), beamline X1 and E4. Detuning the beam intensity to 60% eliminated higher harmonics. The energy of the Pd−K edge was calibrated by using a Pd metal foil measured simultaneously (24350 eV).[45] The energies of the Br−K and Te−L_{III} edges are correspondingly calibrated to the position of the Au−L_{II} edge (13734 eV)[45] of an Au foil and the position of the iodine−L_{III} edge (4557 eV)[45] of a compressed KI pellet. Three ioni-

Table 4. Crystallographic and technical data of the single-crystal X-ray analysis of $Pd_4Br_4Te_3$.

Pearson symbol	$aP22$
space group	$P\bar{1}$
Z	2
a [pm]	842.5(2)
b [pm]	845.0(3)
c [pm]	864.8(3)
α [°]	82.55(3)
β [°]	73.36(2)
γ [°]	88.80(2)
V [pm^3]	584(3)×106
molar mass [$g\,mol^{-1}$]	1128.1
ρ X-ray [$g\,cm^{-3}$]	6.406
μ [mm^{-1}]	27.0
data collection	
crystal size [mm]	0.13×0.15×0.17
diffractometer	STOE IPDS
radiation/monochromator	$Mo_{K\alpha}$/graphite
T [K]	293±5
$\theta_{min}/\theta_{max}$ [°]	3.4/32.8
index range	$-12 \le h \le 12$ $-12 \le k \le 12$ $-13 \le l \le 13$
number of reflections	7730
data reduction	
absorption correction	numerical/X-SHAPE[49]
min/max transmission	0.0215/0.1031
unique reflections	3894
reflections $F_o^2 > 4\sigma(F_o^2)$	3143
R_{int}	0.0281
programs	XCAD-4,[50] XPREP,[51] X-RED[52]
refinement	
minimization function	$\Sigma(F_o^2 - F_c^2)^2(\Sigma^2(F_o^2)+0.027P)^2$ $P=(\max(F_o^2,0)+2/3F_c^2)$
number of variables	101
R_1 [$F_o^2 > 4\sigma(F_o^2)$]	0.0248
R_1 (all)	0.0348
wR_2 (all)	0.0580
goodness of fit	0.938
extinction coefficient	0.00275
$\Delta\rho_{max}$, $\Delta\rho_{min}$ [$\times 10^{-6}\,e\,pm^{-3}$]	1.38, −0.97
program	SHELXL-97[53]

Table 5. Positional and thermal displacement parameters in pm^2 of $Pd_4Br_4Te_3$.

Atom	x	y	z	U_{11}	U_{22}	U_{33}	U_{23}	U_{13}	U_{12}
Pd1	0.42155(5)	0.78322(4)	0.01129(5)	189(2)	209(2)	228(2)	−34(1)	−47(2)	−10(1)
Pd2	0.42501(5)	0.48626(4)	0.29831(5)	249(2)	157(2)	251(2)	−34(1)	−83(2)	−16(1)
Pd3	0.21048(5)	0.44711(4)	0.00250(5)	256(2)	170(2)	270(2)	6(1)	−84(2)	−10(1)
Pd4	0.18306(5)	0.07501(4)	0.33808(4)	197(2)	150(1)	187(2)	13(1)	−37(2)	−38(1)
Br1	0.12927(7)	0.73425(6)	0.01177(8)	212(3)	196(2)	425(3)	−33(2)	−117(3)	0(2)
Br2	0.28252(8)	0.45987(7)	0.69715(7)	268(3)	366(3)	216(2)	−10(2)	−81(2)	−47(2)
Br3	0.33972(8)	0.77876(6)	0.32040(7)	394(3)	180(2)	253(3)	−27(2)	−81(3)	43(2)
Br4	0.11021(7)	0.02560(7)	0.65015(7)	242(3)	373(3)	201(2)	−7(2)	−51(2)	−83(2)
Te1	0.27644(4)	0.15338(3)	0.02477(4)	209(2)	167(1)	198(1)	−17(1)	−60(1)	−24(1)
Te2	0.47793(4)	0.19178(3)	0.29626(4)	203(2)	160(1)	231(2)	−6(1)	−75(1)	−17(1)
Te3	0.14178(4)	0.38412(3)	0.30738(4)	213(2)	174(1)	210(2)	−23(1)	−48(1)	16(1)

zation chambers detected the incident and transmitted flux of the sample and the reference material. The given energies refer to the inflection points of the absorption curves determined from the root of their second derivatives. Each sample was prepared with 30 mg polyethylene and pressed with a force of 10 MN to a pellet of 5 mm in diameter; the sample amounts were 11–24 mg for Pd−*K*, 3–6 mg for Br−*K* and 2.5–4 mg for Te−L_{III}. The mass of sample for the various measurements was chosen such a way that the edge jump reached an relative value of 1–1.5

X-ray diffraction: X-ray powder diffractometry (Philips, X'Pert MPD, Bragg–Brentano, $Cu_{K\alpha}$) was routinely used for phase analysis. The diffraction intensities were usually recorded in the range $5° \leq \theta \leq 90°$ in steps of 0.05° at 8 s per step. The intensity profiles of selected diffractograms were fitted applying the Rietveld method (Figure 2 and Table 3).[47,48] A starting parameter set was generated from the results of a single-crystal structure refinement of $Pd_4Br_4Te_3$. For the details of the single-crystal structure determination (Table 4). The atomic parameters are listed in Table 5; they were also deposited at the Fachinformationszentrum Karlsruhe, D-76344 Eggenstein-Leopoldshafen, Germany, depository Nr. CSD-418003 (Fax +49–7247–808666; e-mail crysdata@fiz.karlsruhe.de).

Theoretical calculations: Extended Hückel calculations were carried out in the tight-binding approximation for 4913 k points equally spread over half of the Brillouin zone using the program YAeHMOP.[54] The crystal orbital overlap populations (COOP) were calculated with a cut-off at 400 pm. The values for ionization potentials H_{ii} (eV), the exponents ζ_1 and ζ_2 in the double expansion of the d orbitals, and the coefficients c_1 and c_2 for Slater type orbitals were used as reported,[54] and are listed in Table 6.

Table 6. Parameters for extended Hückel calculations.

Orbital	H_{ii}	ζ_1	c_1	ζ_1	c_2
Br 4s	−22.07	2.588	–	–	–
Br 4p	−13.10	2.131	–	–	–
Te 5s	−20.80	2.510	–	–	–
Te 5p	−14.80	2.160	–	–	–
Pd 5s	−7.32	2.190	–	–	–
Pd 5p	−3.75	2.152	–	–	–
Pd 4d	−12.02	5.983	0.5264	2.613	0.6373

Acknowledgements

A generous gift of palladium by the former Degussa A.G. is appreciated. The authors thank Samuel Blessing for assisting in the sample preparation.

[1] K. Neininger, H. W. Rotter, G. Thiele, *Z. Anorg. Allg. Chem.* **1997**, *623*, 710–718.
[2] S. V. Volkov, Z. A. Fokina, N. I. Timoshchenko, *Rev. Chim. Min.* **1983**, *20*, 776–785.
[3] M. Paulus, G. Thiele, *Z. Anorg. Allg. Chem.* **1991**, *598*, 253–258.
[4] K. Neininger, G. Thiele, *Z. Anorg. Allg. Chem.* **2002**, *628*, 923–925.
[5] G. Thiele, M. Köhler-Degner, K. Wittmann, G. Zoubek, *Angew. Chem.* **1978**, *90*, 897–898; *Angew. Chem. Int. Ed. Engl.* **1978**, *17*, 853–854.
[6] K. Neininger, H. W. Rotter, G. Thiele, *Z. Anorg. Allg. Chem.* **1996**, *622*, 1814–1818.
[7] H. Ajaz, M. Wagener, C. Reiner, H.-J. Deiseroth, *Z. Kristallogr.* **2006**, *24*, 166.
[8] H. Ajaz, M. Wagener, H.-J. Deiseroth, 13. Fachgruppentagung der Wöhler-Vereinigung für Anorganische Chemie, Aachen, **2006**, Kurzreferate P 064.
[9] D.-K. Seo, M.-H. Whangbo, K. Neininger, G. Thiele, *J. Solid State Chem.* **1998**, *137*, 206–210.
[10] M. Paulus, G. Thiele, *Z. Anorg. Allg. Chem.* **1990**, *588*, 69–76.
[11] L. Wöhler, F. Martin, *Ber. Dtsch. Chem. Ges.* **1909**, *42*, 3958–3965.
[12] L. Wöhler, F. Müller, *Z. Anorg. Allg. Chem.* **1925**, *149*, 377–386.
[13] G. Thiele, P. Woditsch, *Angew. Chem.* **1969**, *81*, 706–707; *Angew. Chem. Int. Ed. Engl.* **1969**, *8*, 672–673.
[14] G. Thiele, M. Steier, D. Wagner, H. Wochner, *Z. Anorg. Allg. Chem.* **1984**, *516*, 207–213.
[15] H.-G. v. Schnering, J.-H. Chang, M. Freiberg, K. Peters, E.-M. Peters, A. Ormeci, L. Schröder, G. Thiele, C. Röhr, *Z. Anorg. Allg. Chem.* **2004**, *630*, 109–116.
[16] J. Fenner, A. Rabenau, G. Trageser, *Adv. Inorg. Chem. Radiochem.* **1980**, *23*, 329–425.
[17] G. Thiele, K. Brodersen, *Fortschr. Chem. Forsch.* **1968**, *10*, 631–673.
[18] K. Brodersen, G. Thiele, H. Gaedecke, *Z. Anorg. Allg. Chem.* **1966**, *348*, 162–167.
[19] C. Wannek, Diplomarbeit, Philipps-Universität Marburg, **1997**.
[20] A. F. Wells, *Z. Kristallogr. Kristallgeom. Kristallphys. Kristallchem.* **1938**, *100*, 189–194.
[21] G. Chattopadhyay, Y. J. Bhatt, S. K. Khera, *J. Less-common Met.* **1986**, *123*, 251–266.
[22] H. Ipser, W. Schuster, *J. Less-common Met.* **1986**, *125*, 183–195.
[23] W. S. Kim, G. Y. Chao, L. J. Cabri, *J. Less-common Met.* **1990**, *162*, 61–74.
[24] F. Grønvold, E. Røst, *Acta Chem. Scand.* **1956**, *10*, 1620–1634.
[25] M. Janetzky, B. Harbrecht, *Z. Anorg. Allg. Chem.* **2004**, *630*, 1732.
[26] M. Janetzky, B. Harbrecht, *Z. Anorg. Allg. Chem.* **2006**, *632*, 837–844.
[27] M. Janetzky, B. Harbrecht, *Z. Kristallogr.* **2005**, *22*, 70 (conference abstract).
[28] Landolt-Börnstein, *Zahlenwerte und Funktionen aus Naturwissenschaften und Technik; Neue Serie, Gruppe II: Atom- und Molekularphysik, Vol. 2, Magnetische Eigenschaften der Koordinations- und metallorganischen Verbindungen der Übergangsmetalle*, Springer, Berlin, **1966**.
[29] H.-G. v. Schnering, J.-H. Chang, K. Peter, E.-M. Peters, F. R. Wagner, Yu. Grin, G. Thiele, *Z. Anorg. Allg. Chem.* **2003**, *629*, 516–512.
[30] D. H. Guthrie, J. D. Corbett, *Inorg. Chem.* **1982**, *21*, 3290–3295.
[31] A. Ritter, T. Lydssan, B. Harbrecht, *Z. Anorg. Allg. Chem.* **1998**, *624*, 1791–1795.
[32] H. Bärnighausen, *MATCH* **1980**, *9*, 139–175.
[33] U. Müller, *Z. Anorg. Allg. Chem.* **2004**, *630*, 1519–1537.
[34] *International Tables for Crystallography, Vol. A1* (Ed.: H. Wondratschek, U. Müller), Kluwer, Dordrecht, **2004**.
[35] S. Jobic, P. Deniard, R. Brec, J. Rouxel, A. Jouanneux, A. N. Fitch, *Z. Anorg. Allg. Chem.* **1991**, *598*, 199–215.
[36] M. Janetzky, B. Harbrecht, unpublished.
[37] A. Bondi, *J. Phys. Chem.* **1964**, 441–451.
[38] A. F. Wells, *Structural Inorganic Chemstry, 5th ed.*, Clarendon, Oxford, **1984**, p. 287.
[39] A. Kjekshus, W. B. Pearson, *Can. J. Phys.* **1965**, *43*, 438–449.
[40] A. Kjekshus, F. Grønvold, *Acta Chem. Scand.* **1959**, *13*, 1767–1774.
[41] Z. Hu, B. Kaindl, G. Meyer, *J. Alloys Compd.* **1998**, *274*, 38–41.
[42] Z. Hu, B. Kaindl, S. A. Warda, D. Reinen, F. M. F. de Groot, B. G. Müller, *Chem. Phys.* **1998**, *232*, 63–74.
[43] Z. Hu, B. Kaindl, B. G. Müller, *J. Alloys Compd.* **1997**, *246*, 177–185.
[44] R. J. Williams, D. R. Dillin, W. O. Milligan, *Acta Crystallogr. Sect. B* **1973**, *29*, 1369–1372.
[45] A. Thompson, D. Vaughan, J. Kirz, D. Attwood, E. Gullikson, M. Howell, K.-J. Kim, J. Kortright, I. Lindau, P. Pianetta, A. Robinson, J. Underwood, G. Williams, H. Winick, *X-Ray data booklet, 2nd ed.*, Lawrence Berkeley National Laboratory, University of California, Berkeley, **2001**.
[46] W. Crawford Dunlop, Jr. in *Methods of Experimental Physics, Vol. 6, Part B* (Eds.: K. L. Horovitz, V. A. Johnson), Academic Press, New York, **1968**, pp. 33.
[47] H. M. Rietveld, *Acta Crystallogr.* **1967**, *22*, 151–152.
[48] H. M. Rietveld, *J. Appl. Crystallogr.* **1969**, *2*, 65–71.

[49] X-SHAPE (2.01), Crystal Optimization for Numerical Absorption Correction, Stoe and Cie, Darmstadt, **2001**.
[50] G. M. Sheldrick, K. Harms, XCAD4 Programm zur LP-Korrektur, Universität Göttingen, **1988**.
[51] XPREP Data Preparation and Reciprocal Space Exploration Ver. 5.05/VMS, Siemens analytical X-ray Insts., **1996**.
[52] X-RED (1.02)-Data Reduction Program, Stoe and Cie, Darmstadt, **2001**.
[53] G. M. Sheldrick, SHELXL-97, A Program Package for the Solution and Refinement of Crystal Structures, Universität Göttingen, **1997**.
[54] G. A. Landrum, W. V. Glassey, YAeHMOP, Yet another extended Hückel Molecular Orbital Package, **1999**.

Received: May 2, 2007
Published online: September 18, 2007

